Simulating an H-type transitional boundary layer in a coupled NLPSE and WMLES framework with a Falkner-Skan wall model

By C. A. Gonzalez, S. R. Harris† AND P. Moin

1. Motivation and objectives

Modeling the transition from laminar to turbulent flow remains a significant challenge in the numerical simulation of boundary layers, especially at coarse grid resolutions. Accurately predicting this transition is crucial for the computation of the drag force, as well as for identifying the state of the boundary layer in areas where flow separation may occur due to the pressure gradient. For example, while increasing the extent of the boundary layer that remains laminar can be advantageous for reducing skin friction, there are situations in which forcing a transition to turbulence is preferable to prevent laminar separation. For high-speed vehicles, boundary-layer transition is associated with large heat transfer from the heated gas to the vehicle surface, which is relevant to the design of thermal protection systems.

Direct numerical simulation (DNS) of the Navier-Stokes (NS) equations is the highest fidelity computational approach for investigating transitional flows. However, its computational cost is unaffordable for practical applications. Sayadi & Moin (2012) found that wall-resolved large-eddy simulations (WRLESs) of H- and K-type transitional boundary layers were able to produce the skin friction overshoot observed in DNS when using dynamic subgrid-scale models. However, these calculations still require a large number of grid points to capture the growth of instabilities. The computational cost of scale-resolving simulations can be further reduced by adopting wall-modeled large-eddy simulations (WMLESs) in which the wall stress is imposed, typically with an equilibrium wall model (EQWM) instead of the classical no-slip boundary condition (Bose & Park 2018). However, most wall models are derived by assuming a fully developed, equilibrium turbulent state. These assumptions result in an incorrect estimation of the momentum loss at the wall in both the laminar and transitional flow regions, leading to inaccuracies in predicting transition behavior. To address this issue, Bodart & Larsson (2012) developed a sensor-based wall model based on the resolved turbulent kinetic energy to switch off the wall model and revert to the no-slip condition when the near-wall flow is detected as laminar. However, a non-universal threshold value for the sensor must be prescribed and DNS-like resolution is required in the laminar and transitional regions of flow to accurately predict the pre-transitional flow. This resolution penalty is severe: Slotnick *et al.* (2014) showed that for external aerodynamic flows, WMLES can require 10–100 times more grid points in the thin laminar region than in the turbulent regime to capture the amplification of disturbances preceding the breakdown to turbulence.

In contrast, linear stability theory (LST) offers a simplified framework to elucidate the evolution of disturbances in the laminar region at significantly reduced computational cost. It can identify dominant instabilities and mechanisms that can lead to nonlinear

† Sandia National Laboratories

interactions downstream as the instabilities amplify. While LST is a potent and commonly employed tool for investigating transitional flows, its scope is restricted to parallel boundary layers and the linear growth of disturbances. The parabolized stability equations (PSEs) introduced by Herbert (1991) and Bertolotti *et al.* (1992) offer a method for studying the evolution of small disturbances in spatially evolving flows. This approach captures the nonparallel effect, enabling more detailed analyses of the spatial growth of disturbances in slowly varying shear flows such as boundary layers, jets and wakes. While both linear and nonlinear forms of the PSE exist, this study focuses on the nonlinear formulation. The nonlinear PSE (NLPSE) accounts for the interactions between modes and their impact on the underlying mean baseflow, with the combined effect of these interactions eventually leading to the breakdown to turbulence. Lozano-Durán *et al.* (2018) demonstrated that coupling an NLPSE solver with an LES code provides a cost-effective and accurate means of computing transitional boundary-layer flows. This work builds upon their findings by employing the Falkner-Skan wall model (FSWM) from Gonzalez *et al.* (2020, 2021) to generate high-resolution laminar baseflow profiles from an initial LES solve of the laminar region of the flow.

2. Governing equations in incompressible flow

We begin by decomposing the primitive variables of velocity and pressure into an averaged baseflow and a perturbation component

$$\phi(x, y, z, t) = \overline{\phi}(x, y) + \phi'(x, y, z, t), \tag{2.1}$$

where

$$\phi = (u, v, w, p)^T. \tag{2.2}$$

We spatially advance two separate systems of equations to capture the evolution of the baseflow $\overline{\phi}$ as well as the perturbations ϕ'.

2.1. *Boundary layer equations*

Averaging the incompressible NS equations in time and assuming the mean flow is homogenous in the spanwise direction yields

$$\frac{\partial \overline{u}_i}{\partial x_i} = 0 \tag{2.3}$$

and

$$\overline{u}_j \frac{\partial \overline{u}_i}{\partial x_j} + \overline{u'_j \frac{\partial u'_i}{\partial x_j}} + \frac{\partial \overline{p}}{\partial x_i} - \frac{1}{\text{Re}} \frac{\partial^2 \overline{u}_i}{\partial x_j \partial x_j} = 0. \tag{2.4}$$

We further assume that the steady-state, two-dimensional baseflow is slowly varying in the wall-parallel direction. Using the standard boundary-layer scaling analysis (White 1974) yields

$$\frac{\partial \overline{u}}{\partial x} + \frac{\partial \overline{v}}{\partial y} = 0, \tag{2.5a}$$

$$\overline{u} \frac{\partial \overline{u}}{\partial x} + \overline{v} \frac{\partial \overline{u}}{\partial y} + \frac{\partial \overline{p}}{\partial x} - \frac{1}{\text{Re}} \frac{\partial^2 \overline{u}}{\partial y^2} = -\left(\overline{u' \frac{\partial u'}{\partial x}} + \overline{v' \frac{\partial u'}{\partial y}} + \overline{w' \frac{\partial u'}{\partial z}} \right), \tag{2.5b}$$

and

$$\frac{\partial \overline{p}}{\partial y} = -\left(\overline{u'\frac{\partial v'}{\partial x}} + \overline{v'\frac{\partial v'}{\partial y}} + \overline{w'\frac{\partial v'}{\partial z}} \right). \tag{2.5c}$$

In both the streamwise and wall-normal momentum equations, we retain the the spanwise and time-averaged nonlinear contribution from the perturbations, which are computed from the mean-flow distortion in the NLPSE.

2.2. *Nonlinear parabolized stability equations*

The equations governing the perturbations ϕ' are derived by taking the difference between the full NS equations and the averaged equations. The resulting system is given by

$$\frac{\partial u'_i}{\partial x_i} = 0 \tag{2.6a}$$

and

$$\frac{\partial u'_i}{\partial t} + \overline{u}_j \frac{\partial u'_i}{\partial x_j} + u'_j \frac{\partial \overline{u}_i}{\partial x_j} + \frac{\partial p'}{\partial x_i} - \frac{1}{\mathrm{Re}} \frac{\partial^2 u'_i}{\partial x_j \partial x_j} = -u'_j \frac{\partial u'_i}{\partial x_j}. \tag{2.6b}$$

The main assumption in the PSE is that in the pre-transitional region of flow, the disturbances can be written as the product of a slowly varying amplitude function and a fast exponential, as in Eq. (2.7),

$$\phi'(x, y, z, t) = \sum_{m=-M}^{M} \sum_{n=-N}^{N} \hat{\phi}_{m,n}(x, y) \exp\left(i \int_{x_0}^{x} \alpha_{m,n}(x')dx' + in\beta z - im\omega t \right). \tag{2.7}$$

In this decomposition, we have assumed that the disturbances are periodic in span and time such that β and ω are the spanwise wave number and the perturbation frequency, respectively. Additionally, $\alpha_{m,n}$ is the streamwise wave number and $\hat{\phi}_{m,n}$ is the amplitude function for the mode described by $(m\omega, n\beta)$.

This decomposition is not uniquely defined, and an extra constraint must be imposed to remove the ambiguity. A commonly used auxiliary condition is

$$\int_0^\infty \hat{\phi}^H \frac{\partial \hat{\phi}}{\partial x} dy = 0, \tag{2.8}$$

which enforces the variation of the amplitude functions to remain small enough to justify the Re^{-1} scaling of $\frac{\partial \hat{\phi}}{\partial x}$ (Schmid & Henningson 2001). Substituting Eq. (2.7) into Eqs. (2.6a) and (2.6b) yields

$$A\hat{\phi}_{m,n} + B\frac{\partial \hat{\phi}_{m,n}}{\partial y} + C\frac{\partial^2 \hat{\phi}_{m,n}}{\partial y^2} + D\frac{\partial \hat{\phi}_{m,n}}{\partial x} + E\frac{\partial \hat{\phi}_{m,n}}{\partial z} + G\frac{\partial^2 \hat{\phi}_{m,n}}{\partial z^2} = \hat{F}_{m,n}, \tag{2.9}$$

where the operators are defined in Appendix A. The iterative solution procedure implemented is described in Appendix B.

3. NLPSE solver verification

As part of this work, a new NLPSE solver has been developed. We verify our solver by applying it to Blasius boundary-layer flows for which there are existing DNS and PSE results in the literature. A Chebyshev differentiation scheme has been implemented for

computing derivatives in the wall-normal direction. The backward Euler method is used for marching the NLPSE in the streamwise direction, and a second-order semi-implicit Crank-Nicholson scheme is used to march the boundary-layer equations. In this section, where we consider the nonlinear evolution of various modes within boundary layers, we adopt the notation (m, n) to denote the harmonic multiple of the modes being plotted. To be exact, m and n are integer multiples of nondimensional temporal and spanwise frequencies, defined as $F = \omega\nu/U_\infty^2 \cdot 10^6$ and $b = \beta\nu/U_\infty \cdot 10^3$. For example, $(1,0)$ corresponds to the mode with temporal frequency F and spanwise frequency zero, $(2,1)$ corresponds to the mode with temporal frequency $2F$ and spanwise frequency b, and $(0,0)$ corresponds to the mean-flow distortion.

3.1. *2D Blasius boundary layer*

The first test case we examine is the nonlinear evolution of a Tollmien-Schlichting (TS) wave in a Blasius boundary-layer flow using the initialization from Bertolotti *et al.* (1992). The disturbance parameters for the TS wave are a nondimensional temporal frequency $F = 86$ and an initial root-mean-squared (rms) amplitude of 0.25% of the freestream velocity. The inlet is specified at $\sqrt{\mathrm{Re}_x} = 400$. In Figure 1, we plot the maximum rms amplitude of the u-velocity perturbation as a function of the streamwise coordinate. Because Bertolotti *et al.* (1992) only report the growth of the first and second harmonics, we include data from Sleeman *et al.* (2023), which also reports the growth of the mean flow distortion. We observe excellent agreement with both the PSE from Bertolotti and the nonlinear, one-way NS result from Sleeman.

3.2. *3D oblique-wave breakdown*

Here we consider the oblique-wave breakdown studied by Joslin *et al.* (1993). This flow is initialized at $\sqrt{\mathrm{Re}_x} = 523$ with a pair of symmetric oblique waves at temporal frequency $F = 86$ and spanwise wave numbers $b = \pm\frac{2}{9}$. The initial rms amplitude of the waves is $A_{1,\pm1} = \sqrt{2} \cdot 10^{-3}$. In Figure 2, we plot the maximum rms amplitude of the u velocity perturbation for various harmonics excited in the flow. Good agreement with the data from Joslin *et al.* (1993) is observed.

3.3. *3D subharmonic-wave breakdown*

Last, we compare our solver to the data from Joslin *et al.* (1993) in the case of subharmonic-wave breakdown. This flow is initialized at $\sqrt{\mathrm{Re}_x} = 426$ with a fundamental TS wave at frequency $F_{2,0} = 124$ and a pair of subharmonic oblique waves with frequency $F_{1,\pm1} = 62$ and spanwise wave numbers $b = \pm0.3303$. The initial rms amplitudes of of the disturbances are $A_{2,0} = 4.8 \cdot 10^{-3}$ and $A_{1,\pm1} = 1.45 \cdot 10^{-5}$. Figure 3 demonstrates that our solver has good agreement with the data from Joslin *et al.* (1993) except near the trailing edge of the flat plate where nonlinear effects quickly increase in magnitude. We attribute these discrepancies to differences in numerics and the initialization procedure.

4. H-type transitional boundary-layer simulations

The setup investigated in this report is a zero-pressure-gradient flat-plate boundary layer from laminar to turbulent flow through an H-type natural transition (Herbert 1991). Unless otherwise stated, velocities are nondimensionalized by the freestream velocity U_∞. LES calculations are carried out using the flow solver charLES, a compressible, unstructured, second-order finite-volume solver with low-dissipation numerics (Bres *et al.* 2018). The dynamic Smagorinski subgrid eddy-viscosity model is used for all charLES
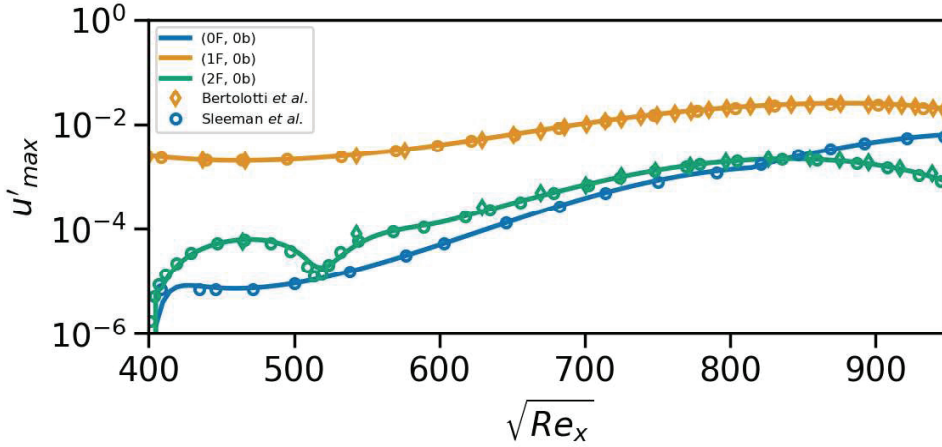
FIGURE 1. Maximum rms amplitude of u' plotted against the streamwise coordinate for the nonlinear evolution of a TS wave at frequency $F = 86$ and initial amplitude of $u'_{max}(x_0) = 0.25\%$.
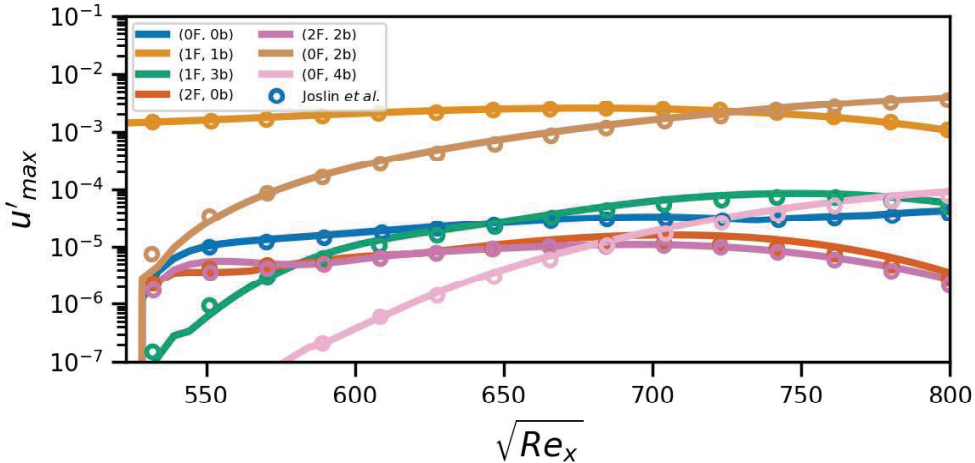

FIGURE 2. Maximum rms amplitude of u' plotted against the streamwise coordinate for oblique-wave breakdown at frequency $F = 86$ and spanwise wave number $b = \frac{2}{9}$, with initial amplitude $u'_{max}(x_0) = \sqrt{2} \times 10^{-3}$.

simulations (Germano *et al.* 1991). The length, height and width of the computational domain are $L_x = 305\delta_0$, $L_y = 30\delta_0$ and $L_z = 20\delta_0$, where δ_0 is the 99% boundary-layer thickness at the inlet. For all LES simulations, hyperbolic tangent stretching is utilized in the wall-normal direction, and uniform spacing is used in the streamwise and spanwise directions. Mesh resolutions for all simulations are given in Table 1. We report the grid spacing with respect to both inner and outer length scales. For the outer length scales, we define the wavelengths
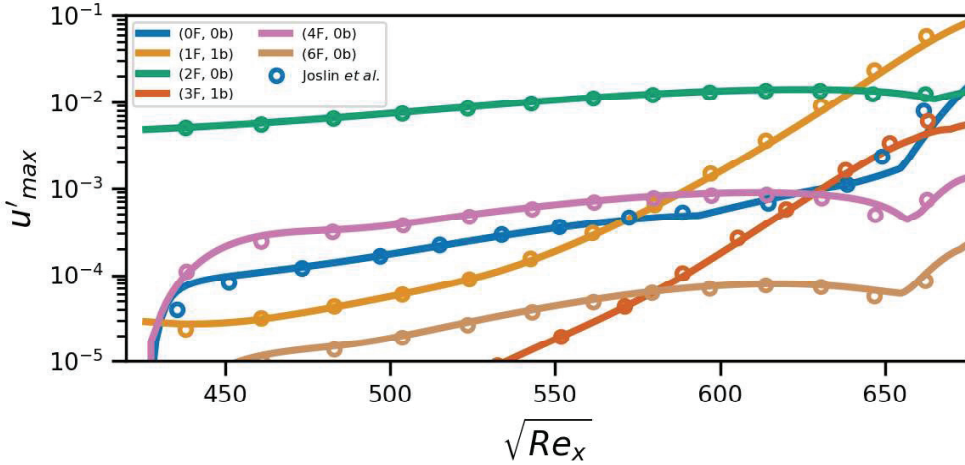
FIGURE 3. Maximum rms amplitude of u' plotted against the streamwise coordinate for subharmonic-wave breakdown. The frequency of the TS wave is set to $F_{TS} = 124$. The frequency of the subharmonic waves is $F = 62$, and the spanwise wave numbers are $b = \pm 0.3303$. The primary wave has an inflow amplitude of $A_{2,0} = 0.0048$ and the subharmonic mode has an inflow amplitude of $A_{1,\pm 1} = 0.145 \cdot 10^{-4}$.

Case	Δx^+	Δy^+	Δz^+	$\frac{\lambda_x}{\Delta x}$	$\frac{\delta_0}{\Delta y}$	$\frac{\lambda_z}{\Delta z}$	N_x	N_y	N_z	N_{cv}
WRLES	30.48	1.06	10.94	32	41	91	1100	300	200	6.6E7
WMLES	61.88	17.39	27.37	15	4	36	650	60	80	3.12E6
CLES	61.88	17.39	27.37	15	4	36	650	60	80	3.12E6
NLPSE/WMLES	54.45	0.33		13	20		250	100	1	2.5E4
NLPSE/**WMLES**	61.88	17.39	27.37	15	4	36	380	60	40	9.12E5

TABLE 1. Mesh resolution in inner and outer scalings for the various cases simulated in this report. Inner units are scaled by the maximum u_τ in the domain. For cases demarked NLPSE/WMLES, the bold text indicates for which side of the simulation mesh data is being presented. 6 temporal modes and 3 spanwise modes are carried in the NLPSE simulation.

$$\lambda_x = \frac{2\pi}{\text{Real}(\alpha_{2,0})} \tag{4.1}$$

and

$$\lambda_z = \frac{2\pi}{\beta}. \tag{4.2}$$

Transition is triggered by imposing an inflow condition consisting of the Blasius solution superposed with disturbances obtained from the linear Orr-Sommerfeld equations. In particular, the disturbances prescribed are a fundamental TS wave and a pair of subharmonic oblique waves at $Re_x = 1.8 \times 10^5$. The nondimensional temporal frequency of the TS wave is $F_{TS} = 124$. The subharmonic frequency is set to $F_{SH} = F_{TS}/2$, and the nondimensional spanwise frequency of the subharmonic disturbances is given by

$b = \pm 0.3303$. Following Joslin *et al.* (1993), the rms amplitudes of the fundamental and subharmonic disturbances are $A_{TS} = 0.0048$ and $A_{SH} = 0.145 \times 10^{-4}$, respectively.

In the work of Lozano-Durán *et al.* (2018), the authors introduce the potential coupling of the NLPSE with WMLES as a method to model transition at an affordable computational cost. In this work, we take one step further by using the FSWM to generate the baseflows used in the NLPSE solver. The motivation behind this is to extend the work further by utilizing the FSWM to generate arbitrarily high-resolution baseflow profiles from the LES, thus further reducing the computational cost of the approach as well as opening the approach to be applied to more complex geometries. As a proof of concept, we generate the initial baseflow used in the NLPSE from an FSWM profile at $Re_x = 1.9 \cdot 10^5$. For WMLESs of aircraft configurations at practical resolutions, it is typical to have fewer than 10 points per boundary layer thickness near the leading edge of surfaces (Bornhoft *et al.* 2022; Goc *et al.* 2022). This level of coarseness in the boundary layer profile cannot support accurate mean baseflows for transition analysis. For example, with 4 points per boundary-layer thickness at the inlet, the coarse large-eddy simulation (CLES) under-predicts the skin friction by almost 10% (Figure 4). An accurate skin friction and decay rate is recovered by $Re_x \approx 4.5e5$, at which point the resolution is approximately 6 points per boundary-layer thickness. However, mean baseflow profiles typically require ~ 30 points per boundary-layer thickness (Choi & Moin 2012) for the accurate computation of stability modes. In contrast, the FSWM is able to accurately predict the skin friction and provide velocity profiles of arbitrary resolution inferred from the inviscid outer flow and an estimation of the boundary-layer thickness from the coarse simulation.

5. Results

Figures 4 and 5 plot the time-averaged skin friction over the whole computational domain, with the DNS data from Lozano-Durán *et al.* (2018) as the reference solution. Also included in these figures are the Blasius laminar boundary-layer skin friction and Prandtl's turbulent stress correlation (White 1974). The WRLES case is refined sufficiently to show reasonable agreement with the skin friction data from the DNS and acts as a benchmark simulation for the performance of charLES for H-type transition. Figure 6 plots instantaneous contours of the u, v and w velocity fields at $y^+ \approx 50$. We see that at this simulation fidelity, the formation of staggered lambda vortices can be observed, which is typical for H-type transition.

The CLES and WMLES are carried out on the same grid, as reported in Table 1. In the case of the WMLES result, the equilibrium wall model is applied along the entire wall. We observe in Figure 7 that the flow transitions near the inlet of the domain, which is also reflected in the skin friction data. Moreover, the velocity contours show that at this mesh resolution, none of the flow structures typical of H-type transition were observed and fine-scale features appear to exist right from the inlet. Qualitatively and quantitatively, this magnitude of misprediction suggests that using WMLES resolution with the EQWM is not a suitable simulation paradigm for transitional flows. In contrast, the CLES case, which applied a no-slip boundary condition on the wall, never transitions; the grid is too coarse to support the disturbances supplied at the inlet of the computational domain. In effect, the flow only sees the mean flow from the imposed Blasius profile.

The setup for the NLPSE/WMLES case begins with an initial run of the boundary-layer flow using the FSWM as the wall boundary condition. Though this case does
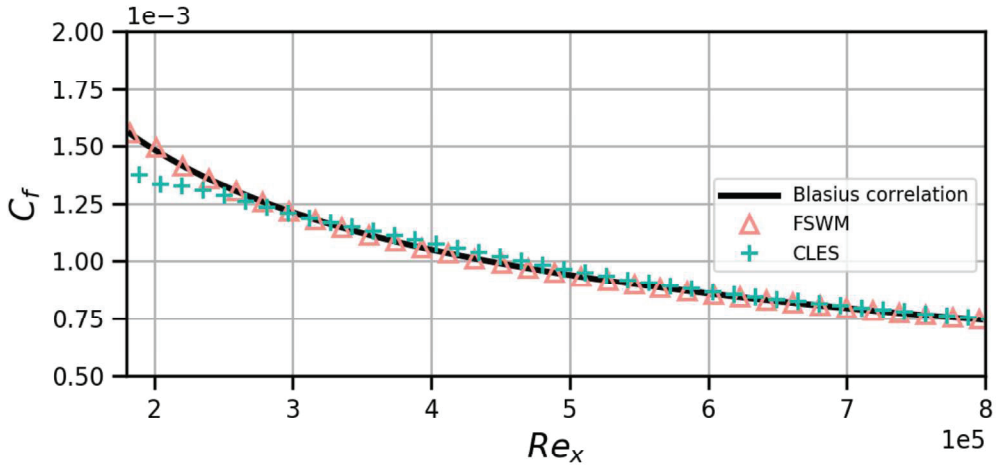
FIGURE 4. Skin friction predictions from coarse LES with a no-slip boundary condition and an FSWM boundary condition.
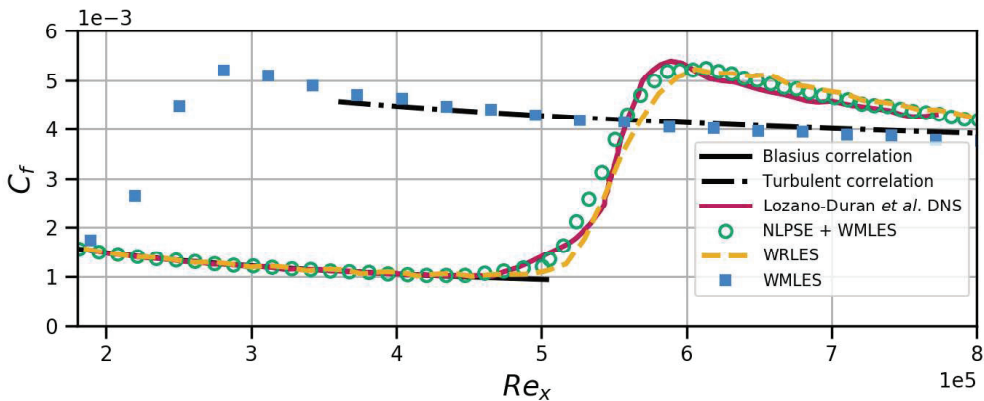

FIGURE 5. Skin friction coefficient as a function of the Reynolds number for a WMLES with the EQWM boundary condition, a WRLES and the proposed NLPSE/WMLES approach.

not transition, the FSWM is able to generate a high-resolution, subgrid boundary-layer profile. The FSWM-generated profile near the inlet is superposed with the disturbances specified above, and the combined profile is used as an inlet condition for our NLPSE solver. The NLPSE solver marches the mean flow and disturbances downstream up to the point of transition. In practice, the NLPSE solver evolves the disturbance equations until it blows up due to the increasingly active non-linear terms; this location is denoted as the point of transition. For this case, the location at which the NLPSE solver is matched to the WMLES is $Re_x = 5 \cdot 10^5$, slightly upstream of the blow-up point of the code. We see that our proposed method of generating a baseflow profile from the FSWM to be marched with the NLPSE and then coupled to a separate WMLES can accurately reproduce the DNS skin friction result (Figure 5). Examining the velocity contours in Figure 8, we see that although there is clear evidence of the lack of resolution in the

Case	Computational Cost (32 CPUs per node)
WRLES	8000 node hours
WMLES	160 node hours
NLPSE/WMLES	30 node hours

TABLE 2. This table shows the computational cost with respect to node hours for the WRLES, WMLES and NLPSE/WMLES calculations.
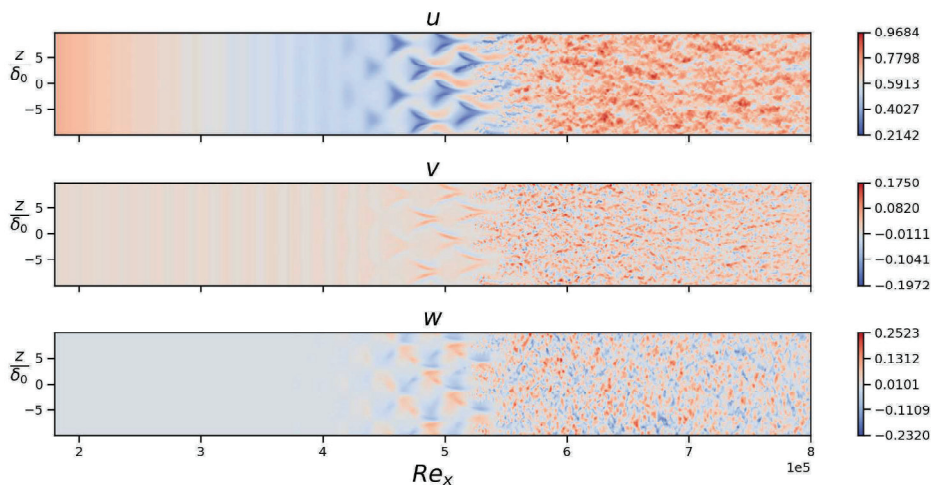

FIGURE 6. u, v and w velocity contours at $y^+ \approx 50$ from the WRLES simulation.

WMLES grid in the downstream portion of the domain, both spanwise and streamwise structures from the NLPSE are retained in the flow. The downstream propagation of these coherent structures is a driving reason why this approach can reproduce the skin friction result from the DNS. The major advantage of this approach, however, is that it comes at a significantly reduced computational cost compared to either the WRLES or DNS, as seen in Table 2.

6. Conclusions

In the present study, we have developed a new nonlinear parabolized stability equation solver to be used as a transition model coupled with WMLESs. This solver has been verified for three canonical transitional flow cases over a flat plate (Herbert 1991; Bertolotti *et al.* 1992; Joslin *et al.* 1993).

We have investigated the capabilities of state-of-the-art LES technology in predicting the zero-pressure-gradient, H-type natural transition scenario. The results of four numerical simulations are reported in this brief using varying modeling assumptions. The DNS data of Lozano-Durán *et al.* (2018) is used for comparison. We showed that WMLES and CLES using the equilibrium wall model and no-slip boundary conditions, respectively, cannot accurately predict the transition behavior of the flow. A WRLES calculation is able to accurately reproduce the DNS skin friction profile, but the resolution and com-
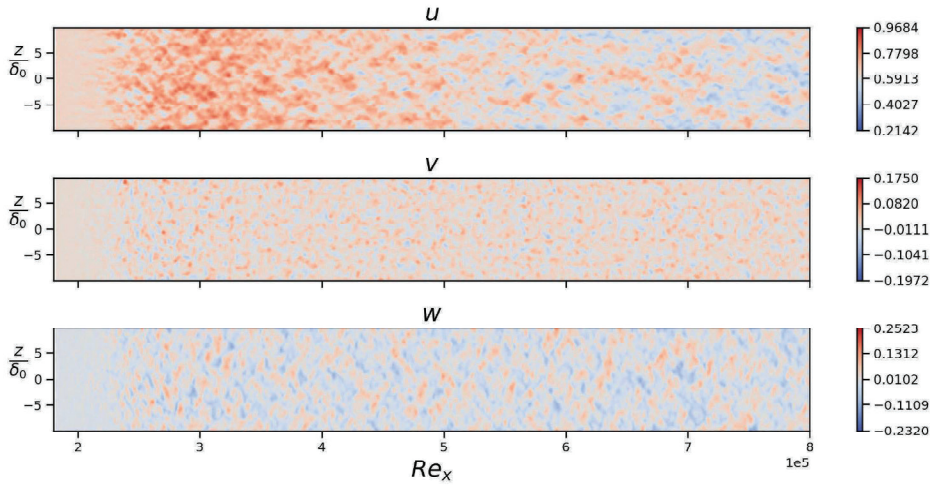
FIGURE 7. u, v and w velocity contours at $y^+ \approx 50$ from the WMLES simulation.
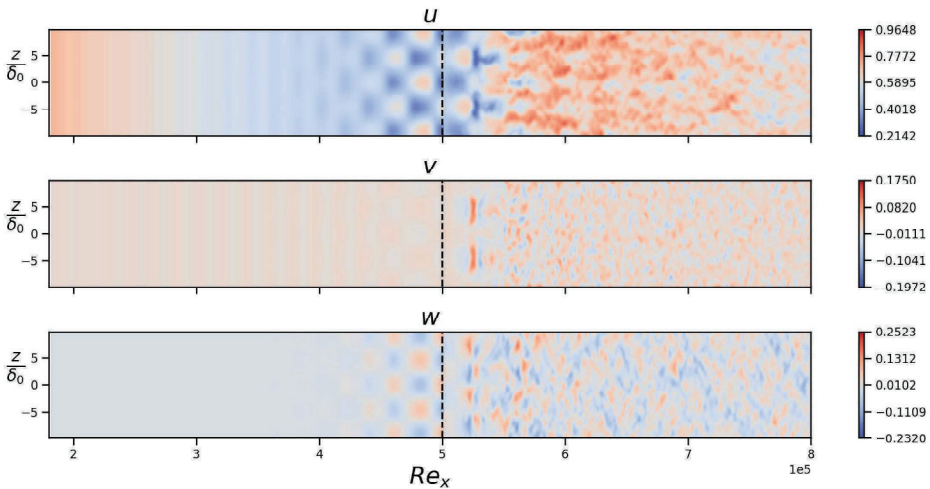

FIGURE 8. u, v and w velocity contours at $y^+ \approx 50$ from the NLPSE/WMLES simulation. The vertical dashed line at $Re_x = 5 \cdot 10^5$ represents the interface between NLPSE and WMLES.

putational cost requirements are too high for practical engineering flows of interest. We demonstrated that using the FSWM on a coarse LES grid is suitable for generating the mean baseflow profiles for the NLPSE solver for this flat plate geometry. Furthermore, the coupled NLPSE/WMLES computation was able to accurately reproduce DNS skin friction profile while attaining a computational cost savings on the order of 250 times as compared with the WRLES.

This work also demonstrates that the NLPSE can be used to generate realistic turbulence inflow conditions. If researchers know the upstream disturbance conditions for a flow of interest, the NLPSE can be used to quickly and cheaply generate conditions sufficient to trigger realistic transition LES calculations.

Acknowledgments

7. Appendix A

The operators for the Cartesian formulation of the nonlinear parabolized stability equations from Eq. (2.9) are given by

$$\Delta = -im\omega + i\alpha_{mn}\overline{u} + \frac{\alpha_{mn}^2}{\text{Re}}, \tag{7.1}$$

$$A = \begin{bmatrix} \Delta + \frac{\partial\overline{u}}{\partial x} & \frac{\partial\overline{u}}{\partial y} & 0 & i\alpha_{mn} \\ 0 & \Delta + \frac{\partial\overline{v}}{\partial y} & 0 & 0 \\ 0 & 0 & \Delta & 0 \\ i\alpha_{mn} & 0 & 0 & 0 \end{bmatrix}, \tag{7.2}$$

$$B = \begin{bmatrix} V & 0 & 0 & 0 \\ 0 & V & 0 & 1 \\ 0 & 0 & V & 0 \\ 0 & 1 & 0 & 0 \end{bmatrix}, \tag{7.3}$$

$$C = \begin{bmatrix} \frac{-1}{\text{Re}} & 0 & 0 & 0 \\ 0 & \frac{-1}{\text{Re}} & 0 & 0 \\ 0 & 0 & \frac{-1}{\text{Re}} & 0 \\ 0 & 0 & 0 & 0 \end{bmatrix}, \tag{7.4}$$

$$D = \begin{bmatrix} U & 0 & 0 & 1 \\ 0 & U & 0 & 0 \\ 0 & 0 & U & 0 \\ 1 & 0 & 0 & 0 \end{bmatrix}, \tag{7.5}$$

$$E = \begin{bmatrix} 0 & 0 & 0 & 0 \\ 0 & 0 & 0 & 0 \\ 0 & 0 & 0 & 1 \\ 0 & 0 & 1 & 0 \end{bmatrix}, \tag{7.6}$$

and

$$G = \begin{bmatrix} \frac{-1}{\text{Re}} & 0 & 0 & 0 \\ 0 & \frac{-1}{\text{Re}} & 0 & 0 \\ 0 & 0 & \frac{-1}{\text{Re}} & 0 \\ 0 & 0 & 0 & 0 \end{bmatrix}. \tag{7.7}$$

Solved for in wave space, the nonlinear forcing term can be expressed in convolutional form as

$$\hat{F}_{m,n}[0] = \sum_{\mu=-M}^{M}\sum_{\nu=-N}^{N} -\left[\hat{u}_{\mu,\nu}\left(i\alpha_{m-\mu,n-\nu}\hat{u}_{m-\mu,n-\nu} + \frac{\partial\hat{u}_{m-\mu,n-\nu}}{\partial x}\right)\right. \tag{7.8a}$$

$$\left. + \hat{v}_{m-\mu,n-\nu}\frac{\partial\hat{u}_{m-\mu,n-\nu}}{\partial y} + \hat{w}_{m-\mu,n-\nu}i\beta_{n-\nu}\hat{u}_{m-\mu,n-\nu}\right]\exp(i\theta_{\mu,\nu} + i\theta_{m-\mu,n-\nu} - i\theta_{m,n}),$$
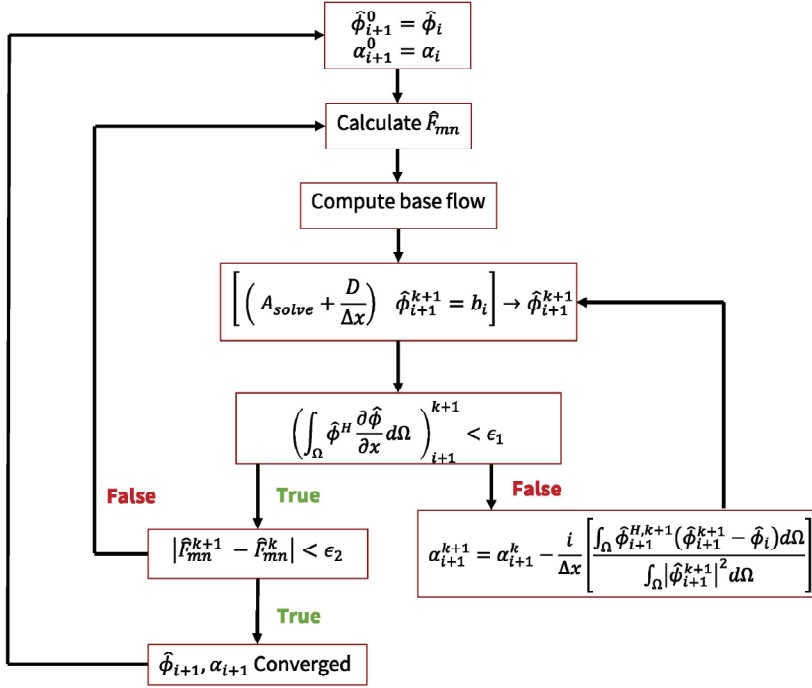
FIGURE 9. Flowchart illustrating the iterative procedure implemented to solve the NLPSE, where $A_{solve} = A + \mathcal{D}_y B + \mathcal{D}_{yy} C + i\beta E - \beta^2 G$ and $b = \frac{D}{\Delta x}\hat{\phi}_i + \hat{F}$.

$$\hat{F}_{m,n}[1] = \sum_{\mu=-M}^{M} \sum_{\nu=-N}^{N} -\left[\hat{u}_{\mu,\nu}\left(i\alpha_{m-\mu,n-\nu}\hat{v}_{m-\mu,n-\nu} + \frac{\partial \hat{v}_{m-\mu,n-\nu}}{\partial x}\right)\right. \tag{7.8b}$$

$$\left. + \hat{v}_{m-\mu,n-\nu}\frac{\partial \hat{v}_{m-\mu,n-\nu}}{\partial y} + \hat{w}_{m-\mu,n-\nu}i\beta_{n-\nu}\hat{v}_{m-\mu,n-\nu}\right]\exp(i\theta_{\mu,\nu} + i\theta_{m-\mu,n-\nu} - i\theta_{m,n}),$$

$$\hat{F}_{m,n}[2] = \sum_{\mu=-M}^{M} \sum_{\nu=-N}^{N} -\left[\hat{u}_{\mu,\nu}\left(i\alpha_{m-\mu,n-\nu}\hat{w}_{m-\mu,n-\nu} + \frac{\partial \hat{w}_{m-\mu,n-\nu}}{\partial x}\right)\right. \tag{7.8c}$$

$$\left. + \hat{v}_{m-\mu,n-\nu}\frac{\partial \hat{w}_{m-\mu,n-\nu}}{\partial y} + \hat{w}_{m-\mu,n-\nu}i\beta_{n-\nu}\hat{w}_{m-\mu,n-\nu}\right]\exp(i\theta_{\mu,\nu} + i\theta_{m-\mu,n-\nu} - i\theta_{m,n}),$$

and

$$\hat{F}_{m,n}[3] = 0, \tag{7.8d}$$

For convenience, we have defined

$$\frac{d\theta_{m,n}}{dx} = \alpha_{m,n}(x). \tag{7.8e}$$

By evaluating the nonlinear terms in wave space, we can avoid dealising procedures.

8. Appendix B

The NLPSE must be solved iteratively to converge the nonlinear forcing terms as well as the shape function $\hat{\phi}$ and growth-rate α. In our solution procedure, we elect to first converge the shape functions and growth rates to a user-specified tolerance ϵ. Once these are converged, the nonlinear forcing terms are recomputed. This procedure is repeated until the forcing terms are within a separately specified tolerance ϵ_2. At the zeroth station for the NLPSE solver, the initial guesses for $\hat{\phi}$ and α are generated from an Orr-Sommerfeld solver. At downstream locations, the initial guesses for the given station i comes from the converged solution at station $i - 1$. This procedure is schematically illustrated in Figure 9.

REFERENCES

BERTOLOTTI, F. P., HERBERT, T. & SPALART, P. 1992 Linear and nonlinear stability of the Blasius boundary layer. *J. Fluid Mech.* **242**, 441–474.

BODART, J. & LARSSON, J. 2012 Sensor-based computation of transitional flows using wall-modeled large eddy simulation. *Annual Research Briefs*, Center for Turbulence Research, Stanford University, pp. 229–240.

BORNHOFT, B., JAIN, S. S., GOC, K., BOSE, S. T. & MOIN, P. 2022 Wall-modeled LES of laser-scanned rime, glaze, and horn ice shapes. *Annual Research Briefs*, Center for Turbulence Research, Stanford University, pp. 71–85.

BOSE, S. T. & PARK, G. I. 2018 Wall-modeled large-eddy simulation for complex turbulent flows. *Annu. Rev. Fluid Mech.* **50**, 535–561.

BRES, G. A., BOSE, S. T., EMORY, M., HAM, F. E., SCHMIDT, O. T., RIGAS, G. & COLONIUS, T. 2018 Large-eddy simulations of co-annular turbulent jet using a Voronoi-based mesh generation framework. In *2018 AIAA/CEAS Aeroacoustics Conference*, p. 3302.

CHOI, H. & MOIN, P. 2012 Grid-point requirements for large eddy simulation: Chapman's estimates revisited. *Phys. Fluids* **24**.

GERMANO, M., PIOMELLI, U., MOIN, P. & CABOT, W. H. 1991 A dynamic subgrid-scale eddy viscosity model. *Phys. Fluids A-Fluid* **3**, 1760–1765.

GOC, K., AGRAWAL, R., BOSE, S. T. & MOIN, P. 2022 Studies in large-eddy simulations of the NASA transonic common research model. *Annual Research Briefs*, Center for Turbulence Research, Stanford University, pp. 13–30.

GONZALEZ, C. A., HARRIS, S. R. & MOIN, P. 2021 Falkner-Skan wall model baseflow generation for the parabolized stability equations. *Annual Research Briefs*, Center for Turbulence Research, Stanford University, pp. 73–81.

GONZALEZ, C. A., KARP, M. & MOIN, P. 2020 Wall-stress modeling for laminar boundary layers in coarse grids. *Annual Research Briefs*, Center for Turbulence Research, Stanford University, pp. 85–95.

HERBERT, T. 1991 Boundary-layer transition-analysis and prediction revisited. In *29th Aerospace Sciences Meeting*, p. 737.

JOSLIN, R. D., STREETT, C. L. & CHANG, C. L. 1993 Spatial direct numerical simulation of boundary-layer transition mechanisms: Validation of PSE theory. *Theor. Comp. Fluid Dyn.* **4**, 271–288.

LOZANO-DURÁN, A., HACK, M. & MOIN, P. 2018 Modeling boundary-layer transition

in direct and large-eddy simulations using parabolized stability equations. *Phys. Rev. Fluids* **3**, 023901.

SAYADI, T. & MOIN, P. 2012 Large eddy simulation of controlled transition to turbulence. *Phys. Fluids* **24**.

SCHMID, P. J. & HENNINGSON, D. S. 2001 *Stability and Transition in Shear Flows.* Springer-Verlag.

SLEEMAN, M. K., LAKEBRINK, M. T. & COLONIUS, T. 2023 Nonlinear stability of wall-bounded flows using the one-way Navier-Stokes (OWNS) equations. *AIAA AVIATION 2023 Forum*, p. 3273.

SLOTNICK, J., KHODADOUST, A., ALONSO, J. & DARMOFAL, D. 2014 CFD Vision 2030 Study: A Path to Revolutionary Computational Aerosciences. *NASA/CR-2014-218178*.

WHITE, F. M. 1974 *Viscous Fluid Flow*, Vol. 3. McGraw-Hill.